Journal of Colloid and Interface Science 716 (2026) 140337

Contents lists available at ScienceDirect

Journal of Colloid And Interface Science

journal homepage: www.elsevier.com/locate/jcis

Synthesis of gold nanorod@Pd(Pt)-Cu_2O dendritic nanocomposites for plasmon-enhanced photocatalysis

Li-Yong Liu [a], Yun-Qi Dou [a], Maarten Bransen [c], Alfons van Blaaderen [c], Tian-Song Deng [a,b,*,1], Xiaoyu Zhao [d], Dechao Yu [e]

[a] School of Electronics and Information Engineering, Hangzhou Dianzi University, Hangzhou, PR China
[b] Key Laboratory of Micro-nano Sensing and IoT of Wenzhou, Wenzhou Institute of Hangzhou Dianzi University, Wenzhou 325038, PR China
[c] Soft Condensed Matter, Debye Institute for Nanomaterials Science, Utrecht University, Utrecht, the Netherlands
[d] College of Materials and Environmental Engineering, Hangzhou Dianzi University, Hangzhou, PR China
[e] School of Optical-Electrical and Computer Engineering & Key Laboratory of Modern Optics System, University of Shanghai for Science and Technology, Shanghai, PR China

GRAPHICAL ABSTRACT

We synthesized gold nanorods@Pd(Pt)-Cu_2O ternary nanocomposites. The AuNR@Pt-Cu_2O showed 35.7× higher photocatalytic activity than Cu_2O alone, due to enhanced charge transfer and photothermal effects. This work advances plasmonic heterostructure design for efficient photocatalysis.

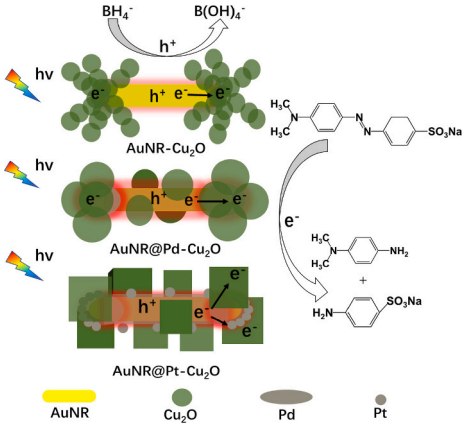

ARTICLE INFO

Keywords:
Gold nanorods
Photocatalysis
Cu_2O
Nanocomposites
Localized surface plasmon resonances
FDTD simulations

ABSTRACT

Combining noble metal nanoparticles with electron acceptors, such as semiconductors or non-plasmonic metals, significantly enhances photocatalytic performance. However, optimizing multi-material combinations for superior catalytic efficiency remains challenging. In this study, we present a method for synthesizing composite structures by reducing Cu^{2+} ions with hydrazine hydrate, forming gold nanorods (AuNRs) decorated with dendritic Cu_2O shells. The influence of CTAB on Cu_2O deposition sites was investigated, and ternary composite nanoparticles were further synthesized by incorporating Pd or Pt into the AuNR-Cu_2O system (AuNR@Pd(Pt)-Cu_2O). The photocatalytic performance of these nanostructures was evaluated by catalyzing methyl orange (MO)

* Corresponding author at: School of Electronics and Information Engineering, Hangzhou Dianzi University, Hangzhou, PR China.
E-mail address: dengts@pku.edu.cn (T.-S. Deng).
[1] orcid.org/0000-0002-0841-4932.

https://doi.org/10.1016/j.jcis.2026.140337
Received 4 January 2026; Received in revised form 10 March 2026; Accepted 18 March 2026
Available online 19 March 2026

under light irradiation. Results showed that AuNR@Pt-Cu_2O nanoparticles exhibited catalytic performance 35.7 times higher than that of pure Cu_2O nanoparticles. This enhancement is attributed to efficient charge transfer and photothermal effects facilitated by the ternary structure. These findings provide valuable insights into plasmonic heterostructure design and open new avenues for developing high-performance photocatalysts for energy and environmental applications.

The increasing severity of global environmental pollution has highlighted the urgent need for solar-powered, environmentally sustainable pollutant degradation. As single materials struggle to meet the evolving demands of advanced photocatalysis, hybrid nanostructures have gained significant attention across multiple scientific disciplines [1–5]. These composite materials not only retain the properties of their individual components but also introduce synergistic effects, leading to new functional capabilities applicable in physics, chemistry, and biomedicine [6–10].

However, the photocatalytic efficiency of metal oxide semiconductor photoelectrodes is often limited by their inherently poor photovoltaic and catalytic properties [11,12]. In contrast, noble metal nanoparticles (NPs), such as gold nanorods (AuNRs), due to their unique localized surface plasmon resonance (LSPR) effect, can generate strong localized electric fields and enable tunable resonance wavelengths. The LSPR of AuNRs can be precisely tuned across the visible and near-infrared regions by adjusting the aspect ratio. These properties allow for effective absorption and conversion of incident energy [13,14]. As a result, combining noble metal NPs with semiconductors can significantly enhance sunlight utilization and accelerate photocatalytic reactions [15,16]. In metal-semiconductor hybrid structures, the Schottky barrier at the interface plays a crucial role in charge separation. However, in n-type semiconductors, this barrier often accelerates electron migration, leading to an imbalance in electron-hole transport rates [17]. In contrast, When Schottky junction is established within a *p*-type semiconductor-metal hybrid structure, it effectively enhances hole migration. Cu_2O, a highly efficient *p*-type semiconductor, when combined with noble metals, creates a Schottky barrier at the interface to facilitate enhanced charge separation during photocatalysis, thereby improving catalytic performance [18–22]. Numerous studies have demonstrated that Au-Cu_2O nanostructures exhibit superior catalytic properties compared to their individual components [20,23–25]. In Au-Cu_2O core-shell nanostructures, methods to improve their catalytic properties usually include the adjustment of Cu_2O crystallinity [26], Cu_2O surface morphology [27], the morphology of Au (spherical [28], rod-like [29], and triangular prisms [30]) and the composite nanostructures [24,28,30]. For example, Dou et al. synthesized Cu_2O-coated AuNRs core-shell structures with different shell thicknesses at low temperatures, achieving a 22-fold increase in catalytic performance compared to bare AuNRs [31]. Similarly, Xu et al. [24] synthesized dumbbell-shaped Au-Cu_2O nanostructures, and found that their photocurrent was approximately 30 times higher than that of Cu_2O nanocubes and 4 times that of AuNR-Cu_2O core-shell structures. Nevertheless, the photocatalytic efficiency of conventional Au-Cu_2O systems is often limited by inefficient charge separation and recombination of photoinduced carriers.

One effective strategy to address this challenge is the introduction of additional catalytic metal components, such as Pd or Pt, into plasmonic-semiconductor systems. These metal can serve as effective electron acceptors and catalytic active sites [32], facilitating hot-electron transfer and accelerating surface redox reaction. AuNRs are often coupled with efficient electron acceptors (e.g., palladium [33–35], platinum [32,36,37],) to maximize the charge separation of hot electrons and thus improve the photocatalytic performances [38–40]. For instance, Guo et al. [34] constructed ordered palladium nanoarrays on AuNRs, demonstrating improved photocatalytic performances by introducing a high density of active sites and extending the lifetime of hot electrons through a Pd nanoarray. Zhang et al. [41] combined plasmonic Au cores with AgPt alloys to form ternary nanostructure, finding that hollow-shell architectures exhibited superior photocatalytic performance, with a reaction rate approximately ~3 times higher than that of the monometallic AuNRs.

Compared to binary metal-semiconductor systems, multi-component nanostructures offer greater flexibility in tuning the size, scale, morphology, and geometric shape to optimize their properties [42–44]. Due to their synergistic effect between different components, these multi-component nanostructures exhibit enhanced catalytic activity and functional versatility [45–47]. For example, Zhu et al. [48] modified the AuNR-TiO_2 dumbbell nanostructure by incorporating Pt NPs as active centers, leading to ~4.3 times higher than that of AuNR-TiO_2. Zhang et al. [49] prepared AgPd@ZIF-8 and AgPd@TiO_2 by selectively coating ZIF-8 and TiO_2 shells onto the AgPd nanodarts. The combination of multiple antimicrobial elements in AgPd@ZIF-8 and photo-generated reactive oxygen species from AgPd@TiO_2 resulted in excellent antimicrobial activities. Although these multi-component composite NPs offer expanded opportunities for tailoring plasmonic functionality, they cannot be achieved simply by physically combining different components. Therefore, promoting photocatalytic reactions by integrating plasmonic metals, catalytically active metals, and semiconductors into ternary nanostructures remains a challenge, as it requires precise control over charge separation and transfer mechanisms.

In this work, we report a controllable synthesis strategy for constructing plasmonic metal-metal-semiconductor hybrid nanostructures based on AuNRs, catalytic metals (Pd or Pt), and Cu_2O. By regulating the concentration of Cu^{2+} precursors, the growth behavior of Cu_2O on AuNRs can be precisely tuned, enabling the formation of distinct morphologies ranging from cubic shells to dendritic structures. Furthermore, ternary nanostructures incorporating Pd or Pt were fabricated to enhance charge transfer and catalytic activity. The optical properties and plasmonic behaviors of these nanostructures were investigated through spectroscopy and finite-difference-time-domain (FDTD) simulations. To evaluate the plasmon-enhanced photocatalytic activity, we employed the reduction of methyl orange as a model reaction under light irradiation. This study provides new insights into the structure-property relationships of multi-component plasmonic photocatalysts and demonstrates an effective strategy for enhancing photocatalytic performance through morphology engineering and multi-metal synergy.

1. Results and Discussion

The schematic illustration of the synthetic route of the AuNR-based dendritic composite NPs was shown in Fig. 1. In brief, the purified AuNRs after washing with water three times, served as the core. A high concentration of freshly prepared N_2H_4 was used as a reducing agent to gradually reduce Cu^{2+} ions at a controlled rate, forming AuNR-Cu_2O NPs. The experimental procedure for synthesizing the composite NPs was shown in Fig. S1. To further enhance the catalytic performance, we introduced different precursors (Na_2PdCl_4, K_2PtCl_4) to the aqueous AuNR solution and used ascorbic acid (AA) as a reducing agent. This resulted in the in-situ deposition of Pd/Pt on the AuNRs, forming AuNR@Pd and AuNR@Pt core-shell nanostructures. Afterwards, the AuNR@Pd and AuNR@Pt NPs served as cores, and Cu^{2+} ions were reduced using the same method, resulting in the formation of a dendritic Cu_2O shell around the core. This Cu_2O shell formation method was also applicable to gold nanoparticles (AuNPs) with different morphologies, demonstrating its universality and broad applicability in plasmonic and

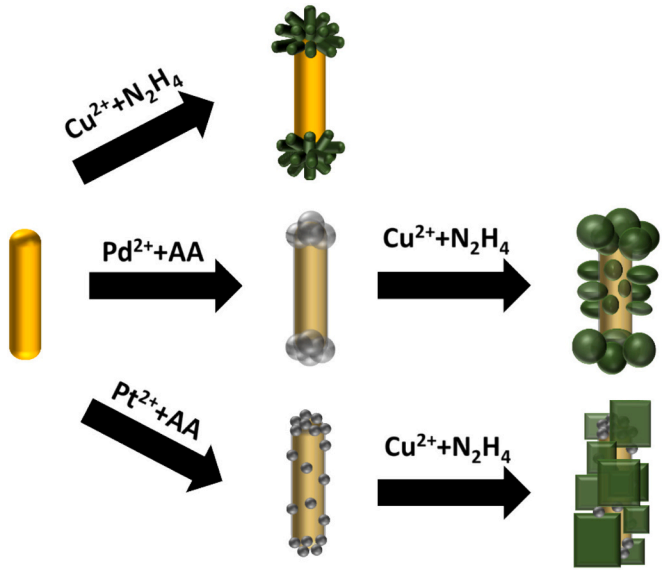

Fig. 1. Schematic illustration of the synthesis route for AuNR-Cu_2O and AuNR@Pd(Pt)-Cu_2O dendritic composite NPs.

catalytic applications.

AuNRs were used as the core due to the adjustable aspect ratio and anisotropic properties, as well as the fact that they do not require further purification after synthesis. NaOL and CTAB were used as binary surfactants to synthesize AuNRs by a seed mediated method [50]. The extinction spectra and the morphological of the synthesized AuNR were shown in Fig. S2, where the average length was 103 nm and the average width was 24 nm, with a narrow longitudinal peak at 848 nm.

To confirm the successful synthesis of composite NPs coated with Cu_2O, the individual AuNR-Cu_2O NPs were further characterized. Fig. 2A shows a high-angle annular dark-field scanning transmission electron microscopy (HAADF-STEM) image of the AuNR-Cu_2O NP, where the brighter rod-like structures in the middle represented the AuNR core, while the dense dendritic structures (darker regions at the ends) represented the Cu_2O shell. Fig. 2B shows the energy dispersive spectroscopy (EDS) mapping, where yellow represents Au, blue represents Cu, and green represents O. It was obvious that Au is distributed in the center of the particle, while Cu and O are distributed in the dendritic shell regions (See Fig. S3).

The synthesized AuNR-Cu_2O NPs exhibited good uniformity and dispersibility, as illustrated in Fig. 2C. Fig. 2D presents high-resolution transmission electron microscopy (HRTEM) image of the AuNR-Cu_2O NPs. By zooming in to observe the interface between Cu_2O and the AuNRs in the red box in Fig. 2E, the measured lattice spacing of the dendritic-like shell were at 2.10 Å and 3.11 Å match the Cu(200) and Cu (110) crystal plane. To further analyze the 3D morphology, electron tomography was performed by tilting the sample holder at angles from −74° to 80° in a transmission electron microscope (TEM), followed by images were processing to generate dynamic images (Video S1) and 3D models (Video S2, Fig. 2F), vividly illustrating the outward branching growth of Cu_2O from the AuNR surfaces. The fast Fourier transform (FFT) analysis further confirmed that dendritic Cu_2O is mainly composed of (200) and (110) crystalline facets (See Supporting Information S3).

N_2H_4 was used to rapidly reduce $Cu(NO_3)_2$ into small Cu_2O NPs [20,25,51], which can quickly aggregate and deposit on rod-shaped NPs, forming a Cu_2O shell layer that epitaxially grew on the AuNR surface [30]. Therefore, to investigate the effect of Cu^{2+} concentration on the

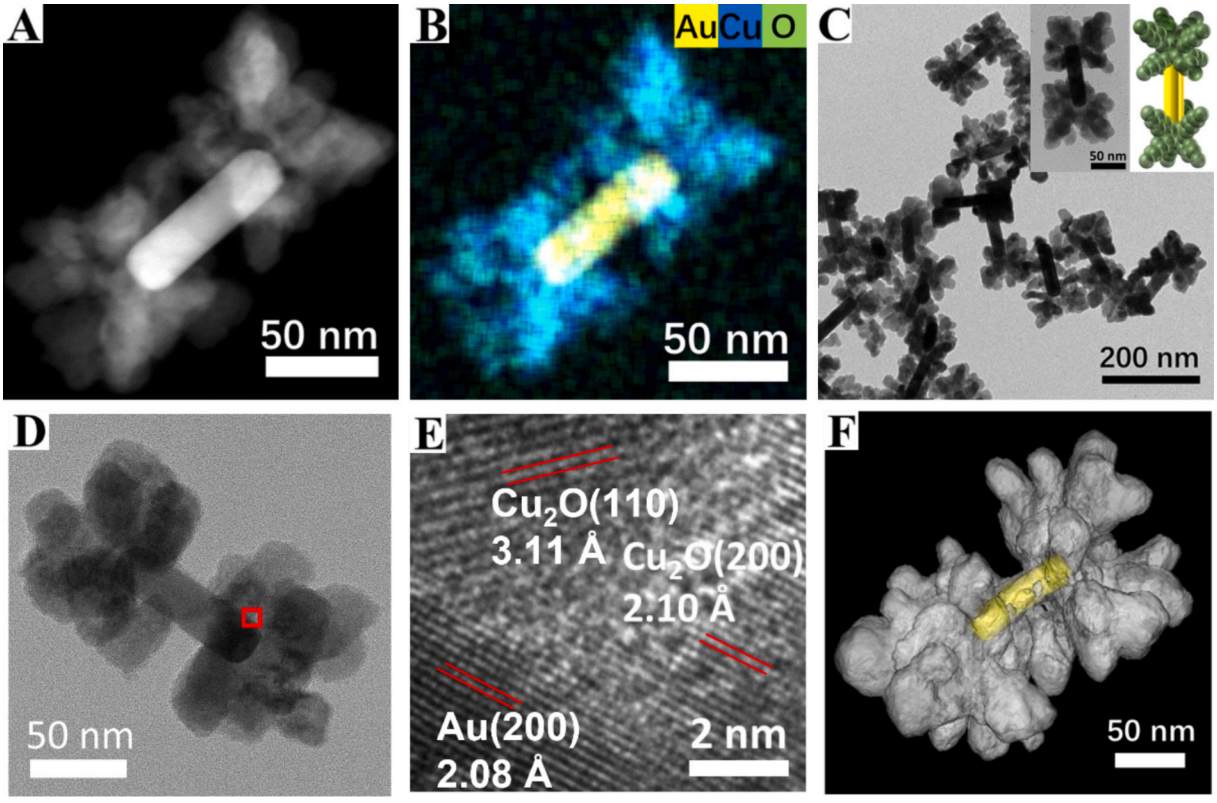

Fig. 2. Dendritic Cu_2O growth at both ends of AuNRs. HAADF-STEM (A) and EDS elemental mapping (B) image of an AuNR-Cu_2O NP. (C) TEM image of AuNR-Cu_2O NPs, with the top-left inset showing a high-magnification TEM image of an individual AuNR-Cu_2O NP and a schematic diagram of the structure. (D) HRTEM image of an AuNR-Cu_2O NP, (E) Lattice fringes at the interface between Au and Cu_2O (enlarged view of the red box in panel D), (F) 3D model of an AuNR-Cu_2O NP reconstructed via electron tomography. (For interpretation of the references to colour in this figure legend, the reader is referred to the web version of this article.)

morphology of Cu_2O shell, nanoparticles with composite structures were synthesized by changing the amount of Cu^{2+} added. Fig. S4 presents the extinction spectra of AuNR-Cu_2O NPs, where narrow absorption peaks are observed in the black curve at 510 nm, 848 nm, corresponding to the transverse and longitudinal absorption peaks of AuNRs. The observed redshift and broadening in the transverse and longitudinal absorption peaks can be attributed to the high refractive index of Cu_2O (≈2.7) [24]. Additionally, a weak absorption at ~450 nm corresponds to the band gap absorption of Cu_2O [23]. As the Cu^{2+} concentration increases, the longitudinal peak underwent a significant redshift.

To systematically investigate Cu_2O shell growth, a fixed volume and concentration of AuNRs were used, while 62.5 mM $Cu(NO_3)_2$ was added in varying volumes (40 μL, 80 μL, 160 μL, 320 μL, and 640 μL). The synthesized NPs were designated as Cu^{2+}: 40 μL, Cu^{2+}: 80 μL, Cu^{2+}: 160 μL, Cu^{2+}: 320 μL, and Cu^{2+}: 640 μL, respectively. TEM images (See Supporting Information S4B—F) confirmed the progressive encapsulation of AuNRs by Cu_2O shells. At lower Cu^{2+} amounts, Cu_2O initially nucleated as small NPs at the ends of the AuNRs. As Cu^{2+} amount increase to 160 μL, the dendritic Cu_2O structures at both ends grow outward significantly, increasing the overall surface area. When the amount of Cu^{2+} reached 320 μL, the Cu_2O morphology transited from a dendritic to a cubic structure at both ends of the AuNRs. Further increasing Cu^{2+} to 640 μL resulted in cube-shaped Cu_2O domains that grow toward the center, ultimately forming a fully covered core-shell structure around the AuNRs. The branched morphology of Cu_2O was believed to arise from concentration depletion effects. Usually, branched structures of crystals are mainly due to both etching and concentration depletion, and Cu_2O typically exhibits a cubic morphology as its dominant crystal habit, with particle size increasing in proportion to the amount of reduced Cu^{2+}. However, during the AuNR-Cu_2O anisotropic growth, only a small fraction of Cu^{2+} was reduced to Cu_2O clusters due to the controlled injection rate and stirring speed of N_2H_4 [23,52]. At 160 μL Cu^{2+}, the limited concentration of reduced Cu_2O clusters led to their rapid consumption at growth sites, forming a concentric diffusion domain around the crystal. At this stage, the Cu_2O concentration at the domain apex was higher than at the center, leading to preferential growth at the ends, resulting in a branching structure. When Cu^{2+} reached 640 μL, the increased concentration of reduced Cu_2O clusters supported the dominance of cubic crystal habit, resulting in the growth of a fully cubic Cu_2O shell [51]. Additionally, to validate this growth mechanism, pure Cu_2O NPs were synthesized under identical conditions using Cu^{2+}: 160 μL. TEM images confirmed that pure Cu_2O also exhibits a dendritic morphology, supporting the hypothesis that branching was induced by concentration depletion rather than etching effects. The extinction spectra and electron microscope images of pure Cu_2O NPs were shown in Fig. S5.

The anisotropic growth of Cu_2O was believed to be influenced by CTAB acting as a soft template, with its distribution typically correlated to the surface curvature of AuNRs. To investigate this effect, a controlled was employed with varying CTAB concentrations to "0" μM, 23.4 μM, and 46.8 μM, respectively. When AuNRs were washed and introduced into Cu^{2+} solution, the CTAB concentration in the solution was approximated as "0" μM. However, a small amount of CTAB molecules that not completely removed during the washing process might still be adhered to the surface of the AuNRs. As a result, AuNRs could still be temporarily stabilized in solution if not vigorously manipulated. The extinction spectra of the resulting samples were shown in Fig. S6A, where the longitudinal plasmonic peak of the AuNRs was observed at 821 nm. When dendritic AuNR-Cu_2O NPs were synthesized at CTAB concentrations of 23.4 μM and 46.8 μM, their longitudinal peaks exhibited redshifts of 242 nm and 270 nm, respectively. In addition, a new peak at 400 nm appeared, which was the characteristic peak of Cu_2O. In contrast, the sample synthesized with "0" μM CTAB maintained its longitudinal peak at 821 nm, while still exhibiting a distinct Cu_2O peak at 400 nm. TEM images of these three samples (See Supporting Information S6B—D) revealed distinct morphological differences. At "0" μM CTAB, dendritic Cu_2O fully covered the AuNRs, forming an AuNR-Cu_2O core-shell structure. It was observed that a few AuNRs still had gaps on both sides, indicating the presence of residual CTAB molecules on their surfaces. At 23.4 μM CTAB, dendritic Cu_2O was mainly deposited on both ends of the AuNRs, resulting in distinct shifts of the longitudinal peaks. At 46.8 μM CTAB, Cu_2O deposition on AuNRs was significantly inhibited, leading to AuNR aggregation. Consequently, the longitudinal peaks broadened rather than shifting. Most Cu_2O particles nucleated independently, forming flower-like Cu_2O NPs, contributing to a pronounced Cu_2O peak at 400 nm. Fig. S7 shows the solution colors of three AuNR-Cu_2O samples. The solution synthesized at 46.8 μM CTAB appeared pale yellow, closely resembling the solution colour of pure Cu_2O NPs, further confirming the autonucleation behavior of Cu_2O. The solution at 23.4 μM CTAB displayed an intermediate hue, with a reddish tint reflecting the presence of AuNRs in the system.

A series of experimental results showed that the concentration of CTAB affects the deposition pattern of Cu_2O. Based on these findings, we hypothesize that the presence of CTAB hinders the deposition of Cu_2O on the AuNRs surface. To further investigate this phenomenon, a surface charge analysis was conducted on the AuNR solution prior to the deposition of dendritic Cu_2O, as shown in Fig. S7B. The Zeta potentials of AuNRs in the solutions containing "0" μM, 23.4 μM, and 46.8 μM CTAB were + 40.7 mV, +45.5 mV, and + 51.2 mV, respectively. The incremental increase in surface potential suggested slight variations in CTAB adsorption on the AuNR surface. These results confirmed that the positive charge imparted by CTAB on AuNRs surface repelled the positively charged Cu^{2+}, resulting in variations in Cu_2O deposition patterns. Additionally, the Zeta potential curve of AuNRs in "0" μM CTAB exhibited a small peak at 10 mV, indicating partial instability due to due to the presence of only a small amount of CTAB. Thus, for optimal synthesis of dendritic AuNR-Cu_2O structures, experiments must be conducted within a short time frame to minimize nanoparticle destabilization.

To further investigate the relationship between Cu_2O deposition patterns and CTAB, we utilized gold nanospheres (AuNSs) and gold nanobipyramids (AuNBPs) as alternative cores for dendritic Cu_2O growth. Following the same synthesis protocol, AuNSs and AuNBPs stored in 0.75 mM CTAB were used in place of AuNRs at an equivalent concentration, ultimately yielding AuNP-Cu_2O dendritic NPs. TEM and spectroscopic measurements were performed to analyze structural and optical changes in these AuNP-Cu_2O nanostructures (Fig. 3).

Fig. 3A depicts the morphology of the AuNSs, showing good size uniformity with an average diameter of 56 nm. The curvature of the edges of the AuNSs remained consistent, and the CTAB molecules were uniformly distributed on their surfaces. Fig. 3B shows the morphology of AuNS-Cu_2O dendritic NPs, aligning with the expected outcome and confirming that dendritic Cu_2O grows uniformly on the AuNSs, forming a sunflower-like structure.

The UV–vis spectra of AuNSs and AuNS-Cu_2O NPs (Fig. 3C) show a 106 nm redshift in the LSPR, accompanied by an increase in intensity. The morphological differences of AuNBPs before and after encapsulation with dendritic Cu_2O were shown in Fig. 3D and E. The average length and width of AuNBPs were approximately 71 nm and 26 nm. Unlike AuNRs, which exhibited high curvature only at the ends, AuNBPs exhibited curvature not only at the ends, but also at the obtuse corners on both sides. Therefore, dendritic Cu_2O deposited not only at the two tips of AuNBPs, but also at the obtuse corners. As shown in Fig. 3F, the UV–vis spectra of AuNBPs and AuNBP-Cu_2O NPs showed a 258 nm redshift of the LSPR and a distinct Cu_2O peak at 400 nm, indicating that Cu_2O deposits on the surface of the AuNPs. In addition, a small fraction of gold nanocubes (AuNCs) formed in the solution during the synthesis of AuNRs (See Supporting Information S8A,). Therefore, the presence of AuNC-Cu_2O NPs was also observed during the deposition of dendritic Cu_2O (See Supporting Information S8B and 8C). Video S3 displays tilt series of HAADF-STEM images of AuNC-Cu_2O NPs, while video S4 presents 3D models reconstructed via electron tomography and image

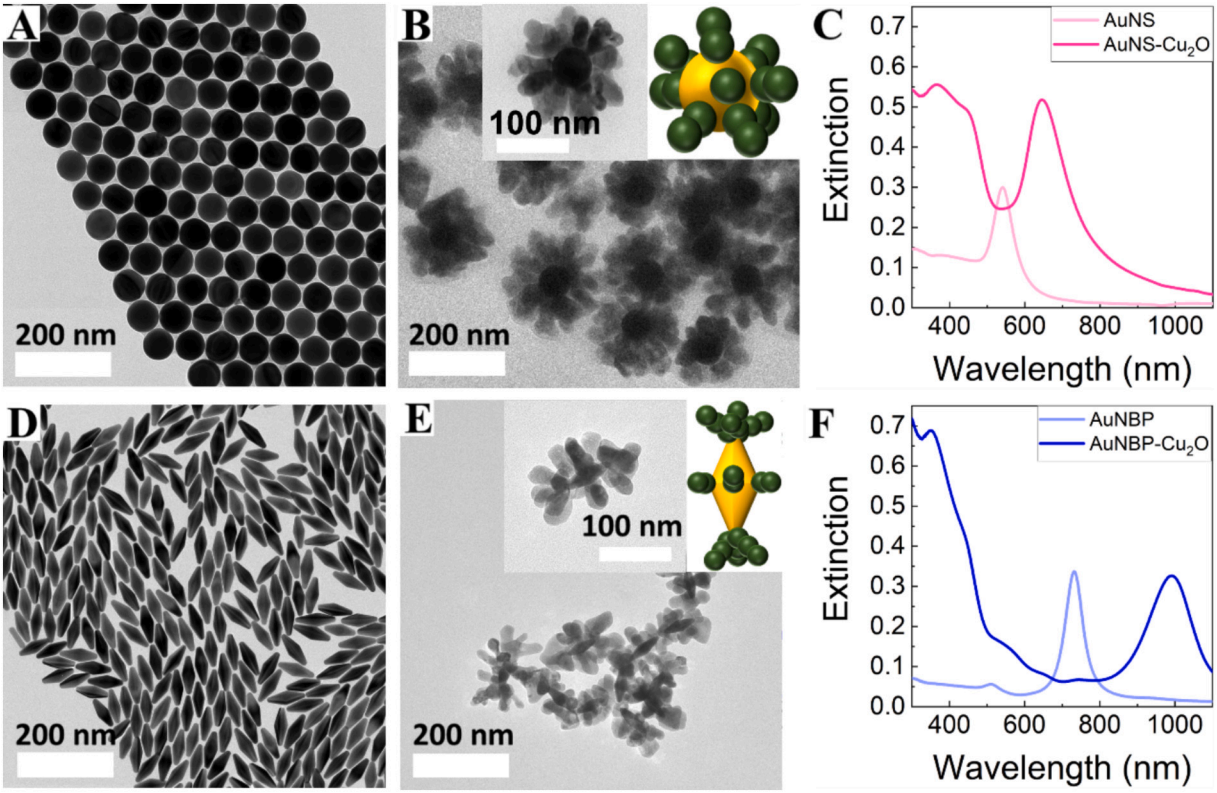

Fig. 3. Selective growth of Cu_2O on AuNP cores with different morphologies. (A) TEM image of AuNSs, (B) TEM image of AuNS-Cu_2O nanocomposites, with the top-left inset showing a high-magnification TEM image of an individual AuNS-Cu_2O NP and a schematic diagram of the structure, (C) UV–vis spectra of AuNSs and AuNS-Cu_2O NPs, (D) TEM image of AuNBPs, (E) TEM image of AuNBP-Cu_2O nanocomposites, with the top-left inset showing a high-magnification TEM image of an individual AuNBP-Cu_2O NP and a schematic diagram of the structure, (F) UV–vis spectra of AuNBPs and AuNBP-Cu_2O NPs. (For interpretation of the references to colour in this figure legend, the reader is referred to the web version of this article.)

processing. It can be observed that the dendritic Cu_2O was preferentially deposited on the eight corners of AuNC, further confirming that the surface curvature of the AuNPs affects the CTAB distribution on AuNP surface, and consequently, directs Cu_2O deposition sites.

The process of dendritic Cu_2O deposition was shown schematically in Fig. S9. When dendritic Cu_2O nanostructures were deposited on different AuNPs, Cu^{2+} ions were preferentially reduced and formed Cu_2O NPs around the AuNPs, which acted like larger particles in the solution. When the CTAB concentration in the solution was about "0" mM, there was no obstruction from CTAB molecules and Cu_2O could be completely deposited on the surface of AuNPs. However, at high CTAB concentrations, the entire AuNP surface was tightly covered by CTAB molecules, which hindered the Cu^{2+} adsorption and made it difficult for Cu_2O to attach to AuNP surface. This led to the self-nucleation of the Cu_2O, leaving bare AuNPs [53]. Within an intermediate CTAB concentration range, CTAB was selectively distributed on the surface of AuNP. Specifically, CTAB molecules packed more densely on flatter surfaces with lower curvature, while they were less tightly packed at tips with higher curvature. The presence of a small number of positively charged CTAB molecules ensured the stability of the AuNPs in solution and repelled the distribution of Cu^{2+} ions on the surface of the AuNPs. As a result, Cu^{2+} ions preferentially accumulated at low-CTAB-content regions, particularly at the tips of AuNPs, thereby influencing the selective deposition of Cu_2O.

In order to further enhance the photocatalytic performance of AuNR-Cu_2O dendritic NPs, a bimetallic structure of AuNR@Pd NPs used as the core. In this process, $PdCl_4^{2-}$ ions were first electrostatically attracted to the positively charged CTAB-coated AuNRs [44]. Subsequently, AA directly served as a reducing agent, resulting in the formation of Pd clusters at the tips of the NRs and altering their extinction spectra and morphology (See Supporting Information S10). Following this step, a Cu_2O shell was grown on the AuNR@Pd NPs, forming the final AuNR@Pd-Cu_2O composite.

The HAADF-STEM shown in Fig. 4A revealed bright rod-like cores, which can be identified as AuNR@Pd. Fig. 4B shows the EDS elemental mapping images of AuNR@Pd-Cu_2O. The EDS maps indicated that the Au was surrounded by Pd and Cu, with Pd clusters predominantly localized at the two ends of the AuNRs, while fewer Pd clusters were found along the lateral surfaces. The combined analysis of the HAADF-STEM and EDS images suggested that Cu is irregularly distributed on the surface of the AuNR@Pd NPs. Fig. 4C displays the HRTEM image of an AuNR@Pd-Cu_2O NP, and Fig. 4D shows a magnified view of the red-marked region in Fig. 4C, highlighting the interface between the Pd shell and the Cu_2O shell in the central structure of the composite. Clearly defined, well-ordered lattice fringes were observed in both the Pd and Cu_2O domains, indicating epitaxial growth at the metal-Cu_2O interface [54]. The measured lattice spacing of d = 2.2 Å corresponds to the (111) crystalline plane of Pd.

In the experiments, we observed that the concentration of Cu^{2+} played an important role in controlling the morphology of Cu_2O. To understand the influence of the concentration of Cu^{2+} on the final morphology, it was adjusted during the growth of the AuNR@Pd-Cu_2O. The extinction spectra of AuNR@Pd-Cu_2O NPs are shown in Fig. S11, where a redshift and broadening of the longitudinal LSPR peaks of the AuNR@Pd-Cu_2O are observed compared to AuNR-Cu_2O. The redshift of these longitudinal LSPR peaks is attributed to the change in tip curvature from AuNR to AuNR@Pd, which facilitated the deposition of a greater number of Cu_2O NPs on the AuNR@Pd surface.

To investigate the effect of Cu^{2+} concentration on shell thickness, a fixed volume and concentration of AuNR@Pd NPs were used, while varying the volume of a 62.5 mM $Cu(NO_3)_2$ solution. The resulting AuNR@Pd-Cu_2O NPs were labeled according to the Cu^{2+} volume added:

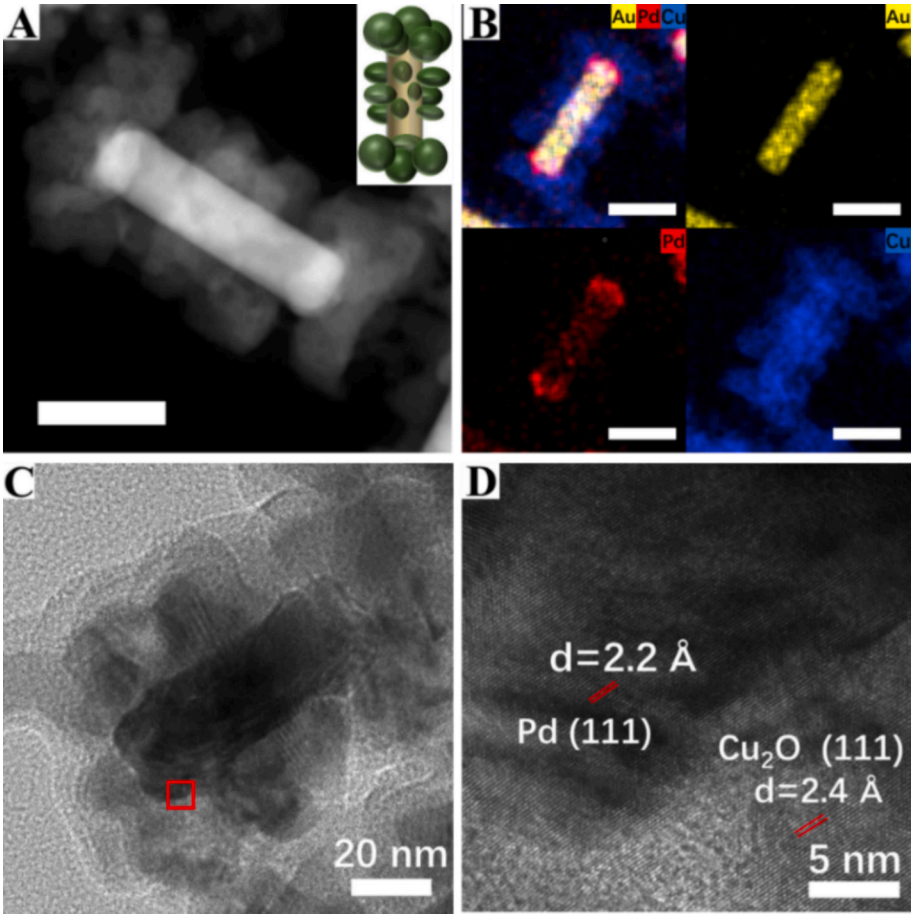

Fig. 4. Synthesis of ternary-structured composite NPs. (A) HAADF–STEM image of an AuNR@Pd-Cu_2O NP, with the top-left inset showing a schematic diagram of its structure. (B) EDS elemental mapping images, illustrating the spatial distribution of Au, Pd and Cu, respectively. (C) HRTEM image of an AuNR@Pd-Cu_2O NP. (D) Magnified HRTEM image of the Pd and Cu_2O interface (red-boxed region in panel C), showing well-defined lattice fringes. (For interpretation of the references to colour in this figure legend, the reader is referred to the web version of this article.)

Cu^{2+}: 40 μL, Cu^{2+}: 80 μL, Cu^{2+}: 160 μL, Cu^{2+}: 320 μL, and Cu^{2+}: 640 μL, respectively. Fig. S11 shows the TEM images of AuNR@Pd cores, which were irregularly coated by Cu_2O NPs, initially appearing as granular deposits. As Cu^{2+} concentration increased, Cu_2O growth progressed from granular deposits at the ends of the nanorods to a cubic morphology encapsulating the entire core. At 640 μL of Cu^{2+}, the Cu_2O NPs formed a well-defined cubic shell, resulting in a complete core-shell structure. The Cu_2O NPs were gradually covered from the ends to the middle, and grew from granular to cubic. When the amount of Cu^{2+} reached 640 μL, Cu_2O in a cubic shape and completely enveloped the core, forming a core-shell structure.

It is worth noting that the growth method of Cu_2O shell is also applicable AuNR@Pt NPs, demonstrating the universality of the approach. To verify this, we replaced the AuNR@Pd with AuNR@Pt. The extinction spectra and TEM images of AuNR@Pt NPs were shown in Fig. S12. Unlike Pd, which exhibited anisotropic growth on AuNR, Pt formed an island like structure due to its stronger cohesive interaction between Pt atoms than the adhesive interaction between Au and Pt atoms. The formed Pt shell inhibited further reaction between $PtCl_4^{2-}$ and the core metal, thereby directing the reaction toward the AuNR side [36,37]. The lattice structure of AuNR@Pt-Cu_2O NPs was shown in Fig. S13, where the lattice spacing of the "Pt islands" is 2.0 Å, closely matching the Pt(200) crystalline plane of 1.96 Å. Similarly, the Cu_2O shell exhibited a lattice spacing of 2.3 Å, corresponding to the Cu(111) plane (2.46 Å) [22]. Fig. S13 also shows the HAADF-STEM and EDS mapping images of AuNR@Pt-Cu_2O NPs. The Cu_2O shell adopted a nearly square morphology and completely encapsulates the AuNR@Pt core. The EDS maps further revealed that Pt forms a core-shell structure around the Au core, with Cu_2O comprising the outermost shell layer.

The UV–vis extinction spectra and TEM images of AuNR@Pt-Cu_2O NPs synthesized with different amounts of $Cu(NO_3)_2$ were shown in Fig. S14. Unlike AuNR@Pd-Cu_2O, the TEM images showed that when only 40 μL of Cu^{2+} was added, there was no significant Cu_2O coating on the AuNR@Pt surface. However, as the Cu^{2+} concentration increased, Cu_2O particles began to grow larger, eventually adopting a cubic morphology. When the addition of Cu^{2+} was 640 μL, the Cu_2O fully covered the AuNR@Pt NP, forming a cubic-shaped shell.

Therefore, we propose that the morphological evolution of the composite NPs is governed by a combination of curvature changes and Cu^{2+} depletion at the AuNR surface. Once the AuNRs were fully coated with Pd shells, their morphology altered: additional Pd clusters preferentially accumulated at the nanorod ends, increasing their surface area. A smaller amount of Pd growth also occurred along the nanorod sides, reducing the curvature contrast between the ends and the middle region. As a result, Cu_2O growth was more pronounced at the ends, but a smaller amount of deposition also occurred in the middle region, leading to the gradual transition from a dumbbell-like structure to a core-shell morphology. In contrast to AuNR-Cu_2O and Au@Pd-Cu_2O, Pt exhibit a unique growth pattern, with Pt forming multiple 'Pt islands' on the AuNR surface. This discontinuous Pt morphology facilitates widespread Cu_2O nucleation, promoting the development of core-shell nanostructures.

Based on the mechanism discussed above, the formation of the dendritic Cu_2O morphology results from the combined effect of CTAB-

mediated interfacial energy regulation and Cu^{2+} concentration. The "Pd clusters" and "Pt islands" in the fully clad metal shell on the surface of AuNRs altered the surface curvature and roughness, resulting in partial disruption of the tightly packed CTAB bilayer on the nanorod sides. This modification enhanced Cu_2O nucleation, providing more favorable growth sites for Cu_2O growth on the nanorod surface.

To further investigate the plasmonic properties of these nanostructures, we performed finite-difference time-domain (FDTD) simulations on the extinction spectra of individual particles under different morphologies (See Supporting Information Fig. S15). Fig. S16 shows the extinction spectra of the nanostructures after modeling them under different morphologies according to the electron microscope images. It

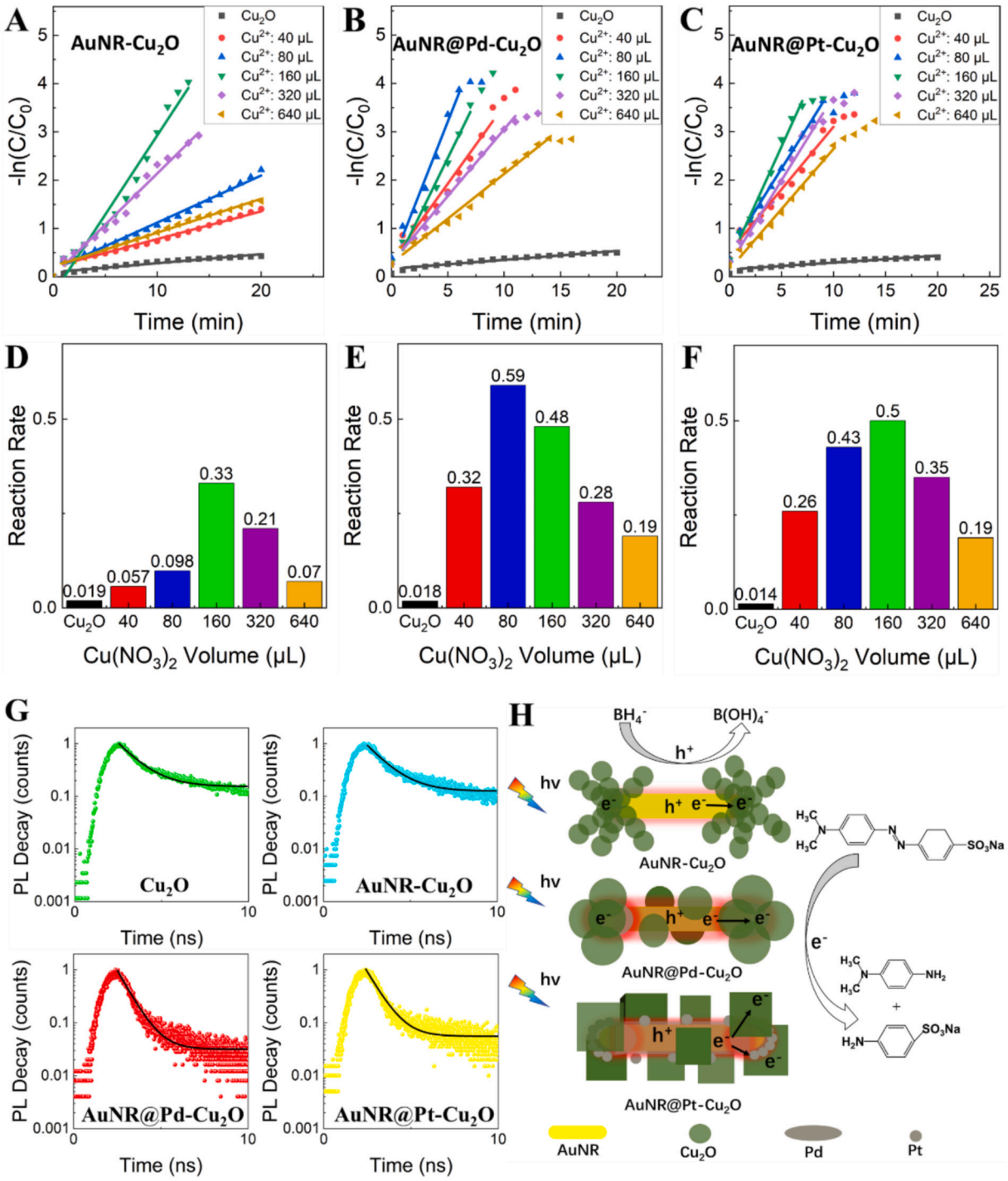

Fig. 5. Ternary structure-enhanced photocatalytic performance. (A, D) Scatter plot of the photocatalytic performance process and rate (slope) bar chart for AuNR-Cu_2O NPs with varying amounts of $Cu(NO_3)_2$. (B, E) Scatter plot of the photocatalytic performance process and rate (slope) bar chart of AuNR@Pd-Cu_2O NPs with varying amounts of $Cu(NO_3)_2$. (C, F) Scatter plot of the photocatalytic performance process and rate (slope) bar chart of AuNR@Pt-Cu_2O NPs with varying amounts of $Cu(NO_3)_2$. (G) TRPL spectra of neat Cu_2O (green), AuNR-Cu_2O (blue), AuNR@Pd-Cu_2O (red) and AuNR@Pt-Cu_2O (yellow) nanostructures. The black curves (from top to bottom) are the fitted curves for Cu_2O, AuNR-Cu_2O, AuNR@Pd-Cu_2O, AuNR@Pt-Cu_2O, recorded at 363 nm excitation and 494 nm emission. (H) Schematic representation of the catalytic reduction mechanism for MO over AuNR-Cu_2O, AuNR@Pd-Cu_2O, and AuNR@Pt-Cu_2O NPs. (For interpretation of the references to colour in this figure legend, the reader is referred to the web version of this article.)

is evident that the longitudinal LSPR peaks of the composite NPs synthesized from AuNR, AuNR@Pd, and AuNR@Pt NP at different Cu^{2+} concentrations are significantly red-shifted. In the simulated spectra, narrower peaks were obtained, while the experimental LSPRs were broadened and attenuated with less redshift than the simulations. This discrepancy arises due to the polydispersity of nanoparticles in aqueous solution and the inherent size variations in experimentally synthesized nanoparticles, whereas the simulation assumed single-particle. Nonetheless, the overall plasmonic peak trend observed in the simulations aligns well with the experimental results.

Ternary nanostructures composed of gold-metal-semiconductor typically exhibit superior catalytic performance compared to binary gold-semiconductor systems [48]. To systematically evaluate the photocatalytic activity of a composite NPs, we selected the reduction of methyl orange (MO) with $NaBH_4$ as a model reaction system under xenon lamp irradiation. The photocatalytic process was monitored through the decolorization of MO aqueous solution from orange to colorless. The degradation kinetics quantified by tracking the temporal evolution of the characteristic absorption peak at 464 nm. A pseudo-first-order kinetic model was applied to the initial rapid reaction phase using the equation: $-\mathrm{Ln}(C/C_0) = kt$, where C_0 represents the initial MO concentration ($t = 0$ min) determined by the peak intensity at 464 nm, C denotes the MO concentration at reaction time t, and k is the rate constant. The photocatalytic performance was further validated through scatter plots and rate constant bar graphs (Fig. 5), with raw catalytic data provided in Supplementary Fig. S17-S27. Notably, control experiments revealed that pure Cu_2O NPs exhibited significantly higher catalytic activity than pure AuNRs (See Supporting Information Fig. S17-S20). Therefore, to isolate the contribution of Cu_2O and establish universal design principles, we maintained a constant Cu^{2+} concentration by adjusting catalyst volumes during photocatalytic testing. Note that in the $NaBH_4$-assisted reduction of methyl orange, $NaBH_4$ provides the chemical reducing.

environment, while light irradiation activates the plasmonic AuNRs, generating hot carriers and localized heating effects. These plasmon-induced processes accelerate electron transfer from $NaBH_4$ to MO through the catalytic interface. Therefore, the enhanced kinetics observed under illumination arise from plasmon-mediated charge transfer and photothermal effects, which go beyond purely chemical reduction by $NaBH_4$.

AuNR-Cu_2O nanostructures were tested as catalysts across varying Cu^{2+} concentrations (40–640 μL, 62.5 mM), with corresponding reaction kinetics shown in Fig. 5A. Pure Cu_2O NPs served as a control baseline for morphology-dependent performance evaluation. As quantified in Fig. 5D and Table S1, the optimal Cu^{2+} volume of 160 μL demonstrated a catalytic rate 17.4-fold higher than pure Cu_2O and 100-fold greater than AuNRs.

The AuNR@Pd-Cu_2O system exhibited distinct catalytic behavior, with scatter plots and rate analysis shown in Fig. 5B and E (See Supporting Information S22, quantitative rates: Table S2,). Control experiments with AuNR@Pd NPs (See Supporting Information S23 and S24) confirmed the synergistic enhancement from Cu_2O integration. Notably, the 80 μL Cu^{2+} condition achieved peak performance, showing a 32.8-fold enhancement over pure Cu_2O and 1.8-fold improvement versus the AuNR-Cu_2O system.

In the AuNR@Pt-Cu_2O system (Fig. 5C and F; Table S3), catalytic optimization occurred at 160 μL Cu^{2+}, contrasting with the Pd-modified counterpart. This configuration yielded a 35.7-fold increase relative to pure Cu_2O and 1.5-fold enhancement compared to AuNR-Cu_2O, surpassing even the Pd-based system. Supplementary Figs. S25-S27 provide full datasets for Pt-containing systems, including control experiments with AuNR@Pt NPs.

Based on the results above, we propose that the AuNR-Cu_2O (Cu^{2+}: 160 μL) with dumbbell structure has superior catalytic performance than that of the AuNR-Cu_2O (Cu^{2+}: 640 μL) with core-shell structure, primarily due to morphological differences. In the core-shell structure, the plasmonic metal was covered with Cu_2O, hindering the interaction of hot carriers with reactants. In contrast, the dumbbell structure facilitated charge separation, allowing hot electrons and holes to participate in oxidation and reduction reactions at distinct active sites [24,30]. Secondly, in AuNR-Cu_2O NPs with a dumbbell morphology, the dendritic Cu_2O structure synthesized with Cu^{2+}: 160 μL exhibited superior catalytic performance compared to the cubic Cu_2O obtained with Cu^{2+}: 320 μL. This enhancement was qualitatively attributed to increased surface roughness and accessible active sites (based primarily on TEM observations) of the dendritic Cu_2O, which promoted MO adsorption and charge transfer [51]. However, the improvement in catalytic performance of AuNR@metal-Cu_2O was attributed to the more frequent electron exchange between core with bimetallic structure and the Cu_2O shell. The introduction of a second metal shell provided an additional energy transfer pathway, complementing the original Au-Cu_2O interface-mediated energy transfer. It was demonstrated that in addition to Cu_2O, Pd and Pt acted as additional electron acceptors in the ternary structure, enhancing the electron transfer and accelerating photocatalytic reactions.

To further verify that the ternary structures enhance charge transfer, we measured the of exciton lifetimes of the AuNR-Cu_2O, AuNR@Pd-Cu_2O, and AuNR@Pt-Cu_2O NPs using time-resolved photoluminescence (TRPL) spectroscopy. The PL decay spectra were recorded on a photoluminescence spectrometer with a 363 nm excitation wavelength. To exclude the influence of Au emissions, only the 494 nm emission was analyzed [55]. We fitted these curves using exponential functions and found that the mono-exponential function could fit the data curves well. The specific formula is as follows:

$$A(t) = A_1 e^{\left(\frac{-t}{\tau_1}\right)} \quad (1)$$

where A_1 represents the initial the initial fluorescence intensity, and τ is the lifetime of excitons in composite NPs. Fig. 5G presents the exciton lifetimes of Cu_2O, AuNR-Cu_2O, AuNR@Pt-Cu_2O and AuNR@Pd-Cu_2O composite NPs. The PL decay curves exhibited a single dominant recombination pathway, and the decay profiles can be well fitted using a mono-exponential model. This indicated that the recombination dynamics were dominated by a primary charge-transfer process at the metal–semiconductor interface. The composite nanostructures exhibited PL decay time within the nanosecond range. The average PL lifetimes of AuNR@Pd-Cu_2O (0.72 ns) and AuNR@Pt-Cu_2O (0.75 ns) were significantly shorter than those of pure Cu_2O NPs (1.15 ns) and AuNR-Cu_2O (1.14 ns), indicating faster charge transfer in the ternary structures.

From these data, it was evident that the catalytic performance of AuNR@Pd-Cu_2O and AuNR@Pt-Cu_2O ternary structured NPs was significantly enhanced compared to AuNR-Cu_2O binary structured NPs. The accelerated PL decay confirmed that charge transfer between the core and the Cu_2O shell was significantly enhanced upon addition of Pd or Pt.

Therefore, we propose the following mechanism of the plasmon-mediated photocatalysis, as illustrated in Fig. 5H. The enhanced photocatalytic performance of the AuNR-based hybrid nanostructures can be attributed to the synergistic interaction between plasmonic excitation, semiconductor charge separation, and catalytic metal sites. Firstly, upon light irradiation, Au nanorods generate LSPR, leading to the formation of energetic hot electrons and strong localized electromagnetic fields near the metal surface. These hot carriers can transfer across the metal–semiconductor interface to the conduction band of Cu_2O, while the remaining holes stay in the Au nanorods. This plasmon-induced charge separation significantly suppresses electron–hole recombination and increases the availability of reactive charge carriers. Secondly, the Cu_2O shell acts as a semiconductor photocatalyst and participates directly in the catalytic reaction. The photogenerated electrons in the Cu_2O conduction band can react with methyl orange molecules or participate in electron transfer processes mediated by $NaBH_4$, thereby

accelerating the reduction reaction. Meanwhile, the presence of dendritic Cu_2O structures increases the surface area and enhances light harvesting, which further improves catalytic performance. Finally, when Pd or Pt is introduced into the system, these metals serve as efficient electron acceptors due to their favorable work functions. Hot electrons generated in the Au nanorods can be rapidly transferred to Pd or Pt domains, where they accumulate and participate in catalytic reactions. This process promotes charge separation and facilitates surface redox reactions at the catalytic metal sites. It partially solves the well-known serious surface charge recombination issue of photocatalysts [56]. In addition, FDTD simulations reveal strong electromagnetic field enhancement at the interfaces between Au nanorods and the Cu_2O structures, particularly in dendritic morphologies. These localized "hot spots" increase the probability of plasmon-induced electron transfer, thereby improving photocatalytic efficiency. Thus, the synergistic effects in ternary AuNR@metal-Cu_2O nanostructures ultimately leads to significantly improved photocatalytic activity.

2. Conclusions

In this work, we developed a controllable strategy for constructing plasmonic metal–metal–semiconductor hybrid nanostructures based on AuNRs, catalytic metals (Pd or Pt), and Cu_2O. By regulating the Cu^{2+} concentration during synthesis, the growth behavior of Cu_2O could be precisely tuned, enabling the formation of distinct morphologies ranging from cubic shells to dendritic structures on the AuNR surface. The experimental results revealed that CTAB-mediated interfacial interactions played a critical role in directing anisotropic Cu_2O growth, which determined the final structural configuration of the composite NPs.

Optical simulations and spectroscopic analyses demonstrated that the morphology of the Cu_2O shell significantly influences the plasmonic properties of the hybrid nanostructures. FDTD simulations confirmed that the dendritic architectures induced pronounced LSPR modulation and enhanced electromagnetic field localization. Furthermore, TRPL measurements indicated that the introduction of Pd or Pt significantly accelerates interfacial charge transfer, leading to more efficient separation of photoinduced carriers.

The plasmon-mediated photocatalytic performance of the synthesized nanostructures was evaluated using the $NaBH_4$-assisted reduction of methyl orange as a model reaction. The dendritic AuNR–Cu_2O nanostructures exhibited a reaction rate 17.4 times higher than that of pure Cu_2O, highlighting the strong plasmonic enhancement effect. More importantly, the ternary AuNR@Pd–Cu_2O and AuNR@Pt–Cu_2O systems further improved catalytic activity, demonstrating 1.8-fold and 1.5-fold higher rates, respectively, compared with the binary AuNR–Cu_2O system. This improvement originated from the synergistic coupling of plasmonic excitation, efficient charge separation at the metal–semiconductor interface, and additional electron extraction provided by the catalytic metal components.

Compared with previously reported Au–Cu_2O hybrid systems, the present work demonstrates that integrating catalytic metal clusters with plasmonic nanorods and semiconductor shells provides a more efficient pathway for tuning charge-transfer processes and enhancing plasmon-driven photocatalysis. The rational design of ternary heterostructures therefore offers a promising approach for overcoming the limitations of conventional binary plasmonic photocatalysts. Thus, this study provides new insights into structure–property relationships in multi-component plasmonic nanostructures and establishes a versatile platform for designing advanced photocatalytic materials. Future work may focus on optimizing the composition and spatial distribution of catalytic metals, as well as extending this strategy to other semiconductor systems and solar-driven catalytic reactions for environmental remediation and sustainable energy conversion.

3. Methods

Chemicals and Materials: All chemicals were used as received without further purification. Hexadecyltrimethylammonium bromide (CTAB, >99%) was purchased from TCI America. L-ascorbic acid (AA, >99.99%), gold(III) chloride hydrate ($HAuCl_4{\cdot}H_2O$, Au ≥48%), sodium tetrachloropalladate(II) (Na_2PdCl_4, 98%), potasium tetrachloroplatinate (II) (K_2PtCl_4, 98%), methyl orange (MO, ≥96%), hydrochloric acid (HCl, 37 wt%), and copper nitrate ($Cu(NO_3)_2$, 99.99%) were purchased from Shanghai Macklin Biochemical Technology Co., Ltd. Sodium borohydride($NaBH_4$, 98%) and silver nitrate ($AgNO_3$, >99.8%) were purchased from Shanghai Aladdin Biochemical Technology Co., Ltd. Hydrazine hydrate (N_2H_4, 64–65%) was purchased from Sigma-Aldrich USA. Sodium hydroxide (NaOH, >96.0%), Ethanol (EtOH, >99.7%) were purchased from Hangzhou Gaojing Fine Chemical Industry Co. Ltd. Ultrapure water (Millipore Milli-Q grade) with a resistivity of 18.2 MΩ was used in all of the experiments.

Synthesis of AuNRs and AuNR-Cu_2O NPs: The AuNRs were synthesized using a previously reported "seed-mediated method" with slight modification [50]. For the seed solution, 0.25 mL of 10.0 mM $HAuCl_4$ and 10 mL of 0.1 M CTAB were mixed in a 20 mL bottle. The freshly prepared ice cold $NaBH_4$ (0.6 mL, 10.0 mM) was quickly added to the mixed solution under vigorous agitation. After the solution became brownish yellow, the stirring was stopped and the solution was left to stand for about 30 min before use. For the growth solution, 7.0 g of CTAB and 1.24 g of NaOL were added in a 500 mL flask, followed by the addition of 250 mL water, after which the solution was magnetically stirred and heated in 50 °C water bath until it was completely dissolved. The solution was cooled down to 30 °C, after which 24 mL of 4.0 mM $AgNO_3$ was added and kept for 15 min, subsequently 25 mL of 10.0 mM $HAuCl_4$ and 225 mL of water were added and the solution was magnetically stirred at 700 rpm for 1 h until the colour of solution faded. 1.5 mL of HCl (37 wt% in water) was added under stirring at 700 rpm for 15 min. After that, 1.25 mL of 64.0 mM AA was added and the mixture was vigorously stirred for 30 s. Finally, 0.8 mL of seed was injected into the mixture with stirring for 30 s. The subsequent rod growth was performed without agitation overnight to obtain AuNRs. The resulting AuNRs had a LSPR wavelength of 752 nm. The final AuNRs were centrifuged at 7155.2 *g* for 15 min, washed once with water, and redispersed in 50 mL of 1.5 mM CTAB.

X μL of 62.5 mM copper nitrate ($Cu(NO_3)_2$) and *Y* ml water were added to a 40 mL glass vial, then 0.3 mL of AuNRs stored in 0.75 mM CTAB were added to the mixture, shaken well, and left standing for 10 min. To grow Cu_2O on AuNR, hydrazine hydrate (N_2H_4) was selected as a strong reducing agent to rapidly reduce Cu^{2+} ions and promote the formation of small Cu_2O nuclei, which subsequently aggregate and grow on the AuNR surface. AuNR-dendritic Cu_2O NPs were obtained by adding 25 vol% hydrazine hydrate (N_2H_4) evenly and slowly at a rate of 0.05 mL/min with a syringe pump for 5 min under 500 rpm magnetic stirring, during which the solution gradually turned light green. CTAB acts as a structure-directing surfactant and stabilizer, controlling nanoparticle dispersion and influencing anisotropic Cu_2O deposition through surface charge interactions. The resulting nanoparticles were immediately centrifuged (11,000 *g*, 5 min), washed with ethanol, and dispersed it in 3 mL of ethanol for storage. The $Cu(NO_3)_2$ volume (*X*) was varied as 40 μL, 80 μL, 160 μL, 320 μL, and 640 μL, corresponding to Cu^{2+}: 40 μL, Cu^{2+}: 80 μL, Cu^{2+}: 160 μL, Cu^{2+}: 320 μL, and Cu^{2+}: 640 μL, respectively. The volume of water (*Y* mL) was adjusted to ensure 32 mL of the total volume.

Synthesis of AuNSs, AuNBPs and AuNP-Cu_2O NPs: The AuNSs were synthesized using a previously reported method [57]. The AuNBPs samples were prepared using a previously reported "seed-mediated growth method" [58]. The synthesis of AuNP-Cu_2O NPs followed the same method as the AuNR-Cu_2O, but the core was changed from AuNRs to AuNSs or AuNBPs.

Synthesis of AuNR@Pd and AuNR@Pd-Cu_2O NPs: The supernatant

was removed by centrifugation of 0.1 mL of prepared AuNRs and dispersed in 3.5 mL of CTAB at a concentration of 30 mM. 50 μL of Na_2PdCl_4 was added at a concentration of 2 mM and shaken to mix. 120 μL of 100 mM AA was added in a 65 °C water bath and left to stand for 30 min. Ascorbic acid (AA) was used as a mild reducing agent during Pd deposition to allow controlled nucleation of metal clusters on the AuNR surface. The obtained AuNR@Pd NPs were centrifuged at 8000 *g* for 15 min, washed once with water, and then dispersed in 0.1 mL of water for storage. Similar to the synthesis of AuNR-Cu_2O NPs described above, 0.3 mL of AuNR@Pd solution in 0.75 mM CTAB was added to $Cu(NO_3)_2$ precursor solutions. The Cu_2O shell was formed following the same method as AuNR-Cu_2O. The resulting particles were immediately washed by centrifugation and stored in ethanol. The final AuNR@Pd-Cu_2O NPs synthesized with five volume of $Cu(NO_3)_2$ was termed as Cu^{2+}: 40 μL, Cu^{2+}: 80 μL, Cu^{2+}: 160 μL, Cu^{2+}: 320 μL, and Cu^{2+}: 640 μL, respectively.

Synthesis of AuNR@Pt and AuNR@Pt-Cu_2O NPs: AuNR@Pt NPs were synthesized using the same method as AuNR@Pd, replacing Na_2PdCl_4 with K_2PtCl_4. AuNR@Pt NPs were washed once with water, and then dispersed them in 0.1 mL of water for storage. The synthesis of AuNR@Pt-Cu_2O NPs was similar to that of AuNR@Pd-Cu_2O NPs mentioned above, except that the core changed from AuNR@Pd to AuNR@Pt.

Characterizations: Optical extinction spectra were recorded with a UV-1900i spectrophotometer (Shimadzu, Japan) with a 10-mm optical path. The TEM images were obtained with an HT-7700 microscope (Hitachi, Japan) operating at a voltage of 100 kV. HRTEM images and EDS mapping were performed using a Talos F200S TEM with a 200 kV acceleration voltage. Time-Resolved Photoluminescence spectra were recorded with a FLS-1000 Spectrometer (Edinburgh, England). The Zeta potential of nanoparticles were measured by dynamic light scattering (DLS, Malvern Zetasizer Nano ZS, UK). The particle sizes of the nanoparticles were measured from TEM images using ImageJ software (v1.53f51), with measurements taken from more than 100 nanoparticles for each sample.

For electron tomography, the dispersion of Au-Cu_2O particles was drop-casted onto a formvar/carbon 75 mesh copper TEM support grid (Ted Pella no. 01802-F, approx. Grid hole size 300 μm) and left to dry under ambient conditions. The grid was then loaded in a single-tilt tomography holder and imaged using a Thermo Fisher Scientific Talos f200x transmission electron microscope operated at 200 kV in HAADF-STEM mode (for tomography, collection angle: 21–127 mrad) or BF-TEM mode (for HR-TEM imaging). Tilt series were recorded for each particle separately using a tilt range of $-74^\circ \leq \theta \leq 80^\circ$ in 2° for increments for $|\theta| \geq 40^\circ$ and 4° increments for $|\theta| < 40^\circ$ at a resolution of 0.52 nm/pixel, with manual focusing at each angle. The tilt-series were aligned using cross-correlation with manual fine-tuning and reconstructed using 20 iterations of the simultaneous iterative reconstruction technique (SIRT) as implemented in the TomoJ software (v2.6) [59]. For segmentation, the reconstructions were smoothed with 3 pixel 3D median filter after which two manually chosen thresholds for the signal intensity were used to segment the Au cores and Cu_2O shells from the background separately, after which a 3 pixel 3D binary opening was applied to the segmented models to remove streaking artefacts from the tomographic reconstruction.

Photocatalysis: The synthesized nanoparticles were washed and centrifuged and dispersed in ultrapure water after twofold dilution. Methyl orange (1 mL, 0.15 mM) and fresh $NaBH_4$ (0.1 mL, 0.05 M) were mixed. Then, different volumes of AuNR-Cu_2O, AuNR@Pd-Cu_2O, and AuNR@Pt-Cu_2O NPs were added to the mixture, and the volume of nanoparticles added was inversely proportional to the volume of Cu^{2+} added during the synthesis of the nanoparticles, with a ratio of 64:1, that is 160 μL, 80 μL, 40 μL, 20 μL, and 10 μL. These catalytic steps were performed under a 250 W xenon lamp (HDL-II, Suzhou Bettick Optoelectronics Technology Co., Ltd., China) illumination. The MO concentration was measured at 465 nm using a UV–visible-near-infrared spectrophotometer (UV-1900i, Shimadzu). The extinction spectra were monitored at 1-min intervals until the peak at 465 nm disappeared and the colour changed from orange to clear. Each reaction was repeated three times to minimize testing errors.

FDTD Simulations: The extinction spectra of AuNR-Cu_2O, AuNR@Pd-Cu_2O, AuNR@Pt-Cu_2O nanostructures were simulated using the finite-difference time-domain (FDTD) method with a software package provided by FDTD Solutions (Lumerical Solutions, Inc. v8.19.1584). The refractive index of the surrounding medium was set to 1.33 (equivalent to water). A perfectly matched layer (PML) was used as the boundary condition. The boundary with NPs inside was divided into a 2 nm mesh size. A total field scattered field source from 300 to 1200 nm wavelength was applied. For size and morphology, the average size determined by TEM measurements were used. For longitudinal excitation, the incident light was perpendicular to the vertical axis and the light was polarized along the long axis of the AuNRs. The dielectric functions of Au, Pd, Pt, and Cu_2O were provided by Palik [60].

Author contribution

T.S.D. initiated the project. L.Y.L. and Y.Q.D. were supervised by T.S.D., while M.B. was supervised by A.v.B. L.Y.L. synthesized AuNRs, Cu_2O, AuNR-Cu_2O, AuNR@Pd, AuNR@Pt, AuNR@Pd-Cu_2O, and AuNR@Pt-Cu_2O NPs. Y.Q.D. synthesized AuNRs, AuNSs, AuNBPs, AuNR-Cu_2O, AuNS@Cu_2O, and AuNBP@Cu_2O NPs. L.Y.L. performed the photocatalytic reactions and FDTD simulations. M.B. conducted electron tomography. L.Y.L., Y.Q.D., and X.Y.Z. carried out HRTEM and EDS mapping. D.C.Y. performed TRPL spectroscopy. L.Y.L., Y.Q.D., and T.S.D. wrote the manuscript. All authors contributed to data analysis and discussions.

CRediT authorship contribution statement

Li-Yong Liu: Writing – review & editing, Writing – original draft, Methodology, Investigation. **Yun-Qi Dou:** Writing – review & editing, Methodology, Investigation. **Maarten Bransen:** Writing – review & editing, Visualization, Methodology. **Alfons van Blaaderen:** Writing – review & editing, Supervision. **Tian-Song Deng:** Writing – review & editing, Supervision, Project administration, Investigation, Funding acquisition, Conceptualization. **Xiaoyu Zhao:** Writing – review & editing, Visualization, Methodology. **Dechao Yu:** Writing – review & editing, Supervision, Methodology, Investigation.

Declaration of competing interest

The authors declare that they have no known competing financial interests or personal relationships that could have appeared to influence the work reported in this paper.

Acknowledgements

The authors thank Ms. Sudan Shen for her assistance in TEM at State Key Laboratory of Chemical Engineering (Zhejiang University). T. S. Deng acknowledge financial support from Zhejiang Provincial Natural Science Foundation (Grant: LY24F050008), and National Natural Science Foundation of China (NSFC, Grant: 61905056). For the electron microscopy the authors acknowledge the UU electron microscopy facility and The Netherlands Electron Microscopy Infrastructure (NEMI), project number 184.034.014, part of the National Roadmap, financed by the Dutch Research Council (NWO).

Appendix A. Supplementary data

Supplementary data to this article can be found online at https://doi.org/10.1016/j.jcis.2026.140337.

Data availability

Data will be made available on request.

References

[1] K. Choi, D. Kim, B. Rungtaweevoranit, C.A. Trickett, J.T.D. Barmanbek, P. Yang, O. M. Yaghi, Plasmon-enhanced photocatalytic CO_2 conversion within metal-organic frameworks under visible light, J. Am. Chem. Soc. 139 (2016) 356–362.

[2] W.B. Hou, S.B. Cronin, A review of surface plasmon resonance-enhanced photocatalysis, Adv. Funct. Mater. 23 (2013) 1612–1619.

[3] M. Kim, M. Lin, J. Son, H.X. Xu, J.M. Nam, Hot-electron-mediated photochemical reactions: principles, recent advances, and challenges, Adv. Opt. Mater. 5 (2017) 1700004.

[4] R. Nebel, K.M. Macounová, H. Tarábková, L. Kavan, P. Krtil, Selectivity of photoelectrochemical water splitting on TiO2 anatase single crystals, J. Phys. Chem. C 123 (2019) 10857–10867.

[5] X.N. Wang, H.J. Zhu, Y.M. Xu, H. Wang, Y. Tao, S. Hark, X.D. Xiao, Q.A. Li, Aligned ZnO/CdTe core-shell nanocable arrays on indium tin oxide: synthesis and photoelectrochemical properties, ACS Nano 4 (2010) 3302–3308.

[6] M. Ha, J.H. Kim, M. You, Q. Li, C. Fan, J.M. Nam, Multicomponent plasmonic nanoparticles: from heterostructured nanoparticles to colloidal composite nanostructures, Chem. Rev. 119 (2019) 12208–12278.

[7] C.L. Ming Zhou, Jiye Fang, Noble-metal based random alloy and intermetallic nanocrystals: syntheses and applications, Chem. Rev. 121 (2021) 736–795.

[8] C.L. Xie, Z.Q. Niu, D. Kim, M.F. Li, P.D. Yang, Surface and interface control in nanoparticle catalysis, Chem. Rev. 120 (2020) 1184–1249.

[9] S. Yoo, J. Lee, H. Hilal, I. Jung, W. Park, J.W. Lee, S. Choi, S. Park, Nesting of multiple polyhedral plasmonic nanoframes into a single entity, Nat. Commun. 13 (2022) 4544.

[10] Q. Zhang, T.S. Deng, M.Z. Wei, X. Chen, Z.Q. Cheng, S.Q. Li, Y.J. Gu, Symmetric and asymmetric overgrowth of a Ag shell onto gold nanorods assisted by Pt pre-deposition, RSC Adv. 11 (2021) 34516–34524.

[11] Y.C. Pu, G.M. Wang, K.D. Chang, Y.C. Ling, Y.K. Lin, B.C. Fitzmorris, C.M. Liu, X. H. Lu, Y.X. Tong, J.Z. Zhang, et al., Au nanostructure-decorated TiO2 nanowires exhibiting photoactivity across entire UV-visible region for photoelectrochemical water splitting, Nano Lett. 13 (2013) 3817–3823.

[12] B.H. Wu, D.Y. Liu, S. Mubeen, T.T. Chuong, M. Moskovits, G.D. Stucky, Anisotropic growth of TiO2 onto gold nanorods for plasmon-enhanced hydrogen production from water reduction, J. Am. Chem. Soc. 138 (2016) 1114–1117.

[13] S. Szunerits, R. Boukherroub, Sensing using localised surface plasmon resonance sensors, Chem. Commun. *48* (2012) 8999–9010.

[14] H.J. Chen, L. Shao, Q. Li, J.F. Wang, Gold nanorods and their plasmonic properties, Chem. Soc. Rev. 42 (2013) 2679–2724.

[15] X.Q. Liu, J. Iocozzia, Y. Wang, X. Cui, Y.H. Chen, S.Q. Zhao, Z. Li, Z.Q. Lin, Noble metal-metal oxide nanohybrids with tailored nanostructures for efficient solar energy conversion, photocatalysis and environmental remediation, Energy Environ. Sci. 10 (2017) 402–434.

[16] W.J. Xu, J. Jia, T. Wang, C. Li, B.W. He, J.P. Zong, Y.W. Wang, H.J. Fan, H.X. Xu, Y. H. Feng, et al., Continuous tuning of au-Cu2O janus nanostructures for efficient charge separation, Angew. Chem. Int. Ed. 59 (2020) 22246–22251.

[17] L.L. Wang, J. Ge, A.L. Wang, M.S. Deng, X.J. Wang, S. Bai, R. Li, J. Jiang, Q. Zhang, Y. Luo, et al., Designing p-type semiconductor-metal hybrid structures for improved photocatalysis, Angew. Chem. Int. Ed. 53 (2014) 5107–5111.

[18] D.H. Jiang, Y.G. Zhang, X.H. Li, Synergistic effects of CuO and au nanodomains on cu_2O cubes for improving photocatalytic activity and stability, Chin. J. Catal. 40 (2019) 105–113.

[19] Chen, X. D.; Cui, K. P.; Hai, Z. B.; Kuang, W.; Wang, L. L.; Zhang, J. J.; Tian, X. Y. Hydrothermal synthesis of cu_2O with morphology evolution and its effect on visible-light photocatalysis. Mater. Lett. 2021, *297*, No. 4.

[20] Y.J. Ma, X.Y. Liu, X.D. Wei, J.M. Le, Y. Fu, Q.Q. Han, H.L. Ji, Z. Yang, H.L. Wu, Single-step coating of mesoporous SiO_2 onto nanoparticles: growth of yolk-shell structures from core-shell structures, Langmuir 37 (2021) 4578–4586.

[21] A. Kumar, H. Singh, S. Sahay, K.B. Balasubramanian, Charge injection into electrodeposited Cu_2O from metallic stacks and graphene, IEEE Trans. Electron Devices 69 (2022) 5755–5759.

[22] H. Zhang, J. Diao, Y. Liu, H. Zhao, B.K.Y. Ng, Z. Ding, Z. Guo, H. Li, J. Jia, C. Yu, et al., In-situ-grown cu dendrites plasmonically enhance electrocatalytic hydrogen evolution on facet-engineered Cu2O, Adv. Mater. 35 (2023) 2305742.

[23] L. Wang, Y. Wu, C. Sun, H. Wang, J. Ren, Shape-controlled Cu_2O nanospheres as bifunctional catalysts boosting the oxidations of glucose and hydrazine, CrystEngComm *23* (2021) 7781–7786.

[24] W. Xu, R. Xiao, S. An, C. Li, J. Ding, H. Chen, H.B. Yang, Y. Feng, Engineering the au-Cu_2O crystalline interfaces for structural and catalytic integration, Small 19 (2023) 2300587.

[25] S.F. Bartolucci, A.C. Leff, J.A. Maurer, Gold-copper oxide core-shell plasmonic nanoparticles: the effect of pH on shell stability and mechanistic insights into shell formation, Nanoscale Adv. 6 (2024) 2499–2507.

[26] M.Y. Kuo, C.F. Hsiao, Y.H. Chiu, T.H. Lai, M.J. Fang, J.Y. Wu, J.W. Chen, C.L. Wu, K.H. Wei, H.C. Lin, et al., Au@Cu_2O core@shell nanocrystals as dual-functional catalysts for sustainable environmental applications, Appl. Catal. B-Environ. 242 (2019) 499–506.

[27] C.H. Kuo, Y.C. Yang, S. Gwo, M.H. Huang, Facet-dependent and au nanocrystal-enhanced electrical and photocatalytic properties of au-Cu2O core-shell heterostructures, J. Am. Chem. Soc. 133 (2011) 1052–1057.

[28] Y.Q. Wang, K. Nikitin, D.W. McComb, Fabrication of au-Cu_2O core-shell nanocube heterostructures, Chem. Phys. Lett. 456 (2008) 202–205.

[29] H. Mahajan, S. Cho, Novel au nanorod/Cu_2O composite nanoparticles for a high-performance supercapacitor, RSC Adv. *12* (2022) 9112–9120.

[30] H.L. Jia, F. Li, T.H. Chow, X.Y. Liu, H. Zhang, Y. Lu, J.F. Wang, C.Y. Zhang, Construction of spatially separated gold nanocrystal/cuprous oxide architecture for plasmon-driven CO2 reduction, Nano Lett. 22 (2022) 7268–7274.

[31] Y.Q. Dou, T.S. Deng, Q. Zhang, X.Y. Zhao, J. Liu, Z.Q. Cheng, A study of size-controlled au@Cu_2O nanocomposite for highly improved methyl orange catalytic performances, J. Mater. Sci. 58 (2023) 7583–7593.

[32] Z.K. Zheng, T. Tachikawa, T. Majima, Single-particle study of Pt-modified au nanorods for plasmon-enhanced hydrogen generation in visible to near-infrared region, J. Am. Chem. Soc. 136 (2014) 6870–6873.

[33] R. Long, Z.L. Rao, K.K. Mao, Y. Li, C. Zhang, Q.L. Liu, C.M. Wang, Z.Y. Li, X.J. Wu, Y.J. Xiong, Efficient coupling of solar energy to catalytic hydrogenation by using well-designed palladium nanostructures, Angew. Chem. Int. Ed. 54 (2015) 2425–2430.

[34] J. Guo, Y. Zhang, L. Shi, Y.F. Zhu, M.F. Mideksa, K. Hou, W.S. Zhao, D.W. Wang, M. T. Zhao, X.F. Zhang, et al., Boosting hot electrons in hetero-superstructures for plasmon-enhanced catalysis, J. Am. Chem. Soc. 139 (2017) 17964–17972.

[35] X. Zhu, H. Jia, X.M. Zhu, S. Cheng, X. Zhuo, F. Qin, Z. Yang, J. Wang, Selective Pd deposition on au nanobipyramids and Pd site-dependent plasmonic photocatalytic activity, Adv. Funct. Mater. 27 (2017) 1700016.

[36] J. Fennell, D.S. He, A.M. Tanyi, A.J. Logsdail, R.L. Johnston, Z.Y. Li, S.L. Horswell, A selective blocking method to control the overgrowth of Pt on au nanorods, J. Am. Chem. Soc. 135 (2013) 6554–6561.

[37] Y. Rong, A. Dandapat, Y.J. Huang, Y. Sasson, L. Zhang, L.W. Dai, J.W. Zhang, Z. Y. Guo, T. Chen, Spatially-controlled growth of platinum on gold nanorods with tailoring plasmonic and catalytic properties, RSC Adv. 6 (2016) 10713–10718.

[38] X.B. Xie, M.A. van Huis, A. van Blaaderen, Symmetric and asymmetric epitaxial growth of metals (ag, Pd, and Pt) onto au nanotriangles: effects of reductants and plasmonic properties, Nanoscale 13 (2021) 2902–2913.

[39] M. Lv, X.X. Zhang, B. Li, X.Q. Gong, Y.J. Zhang, Z.Y. Wang, Y.Y. Liu, P. Wang, H. F. Cheng, Y. Dai, et al., Plasmonic ag interlayer induced direct energy transfer studied at single-particle level, ACS Energy Lett. 8 (2023) 4033–4042.

[40] E.J. Zhang, T.S. Deng, Y.C. Cheng, L.Y. Liu, J.F. Gao, J.H. Wen, X.Y. Zhao, J. Liu, Gold nanobipyramids coated with silver-platinum alloy shells for plasmonically enhanced photocatalytic degradation of methyl orange, ACS Appl. Nano Mater. 7 (2024) 14596–14608.

[41] Q. Zhang, T.S. Deng, Y.Q. Dou, M.Z. Wei, S.Q. Li, J. Liu, Z.Q. Cheng, Trimetallic nanostructures of silver-platinum alloy shells on gold nanorods for plasmon-mediated photocatalysis, ACS Appl. Nano Mater. 5 (2022) 17048–17058.

[42] W. Gao, C. Kan, S. Ke, Q. Yun, X. Zhu, X. Zhu, Au nanobipyramids with Pt decoration enveloped in TiO_2 nanoboxes for photocatalytic reactions, Nanoscale Adv. *3* (2021) 4226–4234.

[43] J.E.S. van der Hoeven, J. Jelic, L.A. Olthof, G. Totarella, R.J.A. van Dijk-Moes, J. M. Krafft, C. Louis, F. Studt, A. van Blaaderen, P.E. de Jongh, Unlocking synergy in bimetallic catalysts by core-shell design, Nat. Mater. 20 (2021) 1216–1220.

[44] Y.H. Zhao, R.M. Sarhan, A. Eljarrat, Z. Kochovski, C. Koch, B. Schmidt, W. Koopman, Y. Lu, Surface-functionalized au-Pd nanorods with enhanced photothermal conversion and catalytic performance, ACS Appl. Mater. Interfaces 14 (2022) 17259–17272.

[45] H.D. Ha, C. Yan, G. Katsoukis, G.A. Kamat, I.A. Moreno-Hernandez, H. Frei, A. P. Alivisatos, Precise colloidal plasmonic photocatalysts constructed by multistep photodepositions, Nano Lett. 20 (2020) 8661–8667.

[46] X. Liu, J.T. Han, X.P. Qiao, H.J. Cai, Y. Zhao, Z.H. Zhang, B.Q. Zhai, T.J. Ni, C. Zhao, Y.H. Zhu, Bimetallic au and Pd nanoparticles modified WO3 nanosheets for enhancing the sensitivity and selectivity of formaldehyde assessment in aquatic products, ACS Appl. Mater. Interfaces 16 (2024) 22155–22165.

[47] W. Albrecht, J.E.S. van der Hoeven, T.S. Deng, P.E. de Jongh, A. van Blaaderen, Fully alloyed metal nanorods with highly tunable properties, Nanoscale 9 (2017) 2845–2851.

[48] M.T. Zhu, Y.Y. Wang, Y.H. Deng, X.N. Peng, X.N. Wang, H. Yuan, Z.J. Yang, Y. L. Wang, H. Wang, Strategic modulation of energy transfer in au-TiO2-Pt nanodumbbells: plasmon-enhanced hydrogen evolution reaction, Nanoscale 12 (2020) 7035–7044.

[49] Zhang, H.; Lu, Y.; Zhang, R.; Tang, Z.; Lam, S. H.; Zhu, J. J.; Fu, R. F.; Hu, Y. T.; Iqbal, M. Z.; Kong, X. D.; et al. Synthesis of multifunctional plasmonic nanodarts through one-end deposition on gold nanobipyramids for tumor organoid ablation and antimicrobial applications. Adv. Funct. Mater. 2024, No. 15.

[50] X.C. Ye, C. Zheng, J. Chen, Y.Z. Gao, C.B. Murray, Using binary surfactant mixtures to simultaneously improve the dimensional tunability and monodispersity in the seeded growth of gold nanorods, Nano Lett. 13 (2013) 765–771.

[51] J.W. Liu, F.T. You, B.W. He, Y.L. Wu, D.D. Wang, W.Q. Zhou, C. Qian, G.B. Yang, G. F. Liu, H. Wang, et al., Directing the architecture of surface-clean Cu2O for CO electroreduction, J. Am. Chem. Soc. 144 (2022) 12410–12420.

[52] J.W. Liu, S.Y. Wang, K. Cai, Y.F. Li, Z.P. Liu, L.M. Liu, Y. Han, H. Wang, H.Y. Han, H.Y. Chen, A new type of capping agent in nanoscience: metal cations, Small 15 (2019) 1900444.

[53] G.L. He, Y.H. Lai, Y.Z. Guo, H. Yin, B.B. Chang, M. Liu, S.R. Zhang, B.C. Yang, J. F. Wang, Tipping gold nanobipyramids with titania for the use of plasmonic hotspots to drive amine coupling, ACS Appl. Mater. Interfaces 14 (2022) 53724–53735.

[54] N. Meir, I.J.L. Plante, K. Flomin, E. Chockler, B. Moshofsky, M. Diab, M. Volokh, T. Mokari, Studying the chemical, optical and catalytic properties of noble metal (Pt, Pd, Ag, Au)-Cu2O core-shell nanostructures grown via a general approach, J. Mater. Chem. A 1 (2013) 1763–1769.
[55] W.J. Xu, R.X. Xiao, S.Y. An, C. Li, J. Ding, H.Y. Chen, H.B. Yang, Y.H. Feng, Engineering the Au-Cu2O crystalline interfaces for structural and catalytic integration, Small 19 (2023) 11.
[56] M. Xiao, Z.L. Wang, M.Q. Lyu, B. Luo, S.C. Wang, G. Liu, H.M. Cheng, L.Z. Wang, Hollow nanostructures for photocatalysis: advantages and challenges, Adv. Mater. 31 (2019) 23.
[57] Q.F. Ruan, L. Shao, Y.W. Shu, J.F. Wang, H.K. Wu, Growth of monodisperse gold nanospheres with diameters from 20 nm to 220 nm and their core/satellite nanostructures, Adv. Opt. Mater. 2 (2014) 65–73.
[58] A. Sánchez-Iglesias, N. Winckelmans, T. Altantzis, S. Bals, M. Grzelczak, L.M. Liz-Marzán, High-yield seeded growth of monodisperse pentatwinned gold nanoparticles through thermally induced seed twinning, J. Am. Chem. Soc. 139 (2017) 107–110.
[59] C. Messaoudil, T. Boudier, C.O.S. Sorzano, S. Marco, TomoJ: tomography software for three-dimensional reconstruction in transmission electron microscopy, BMC Bioinformatics 8 (2007) 9.
[60] E.J. Prucha, E.D. Palik, Handbook of Optical Constants of Solids, Academic Press, 1998.